Arabian Journal of Chemistry (2022) **15**, 103613

King Saud University

**Arabian Journal of Chemistry**

www.ksu.edu.sa
www.sciencedirect.com

ORIGINAL ARTICLE

# Facile synthesis and characterization of $Fe_2O_3$ nanoparticles using L-lysine and L-serine for efficient photocatalytic degradation of methylene blue dye

**Abdu Subaihi** [a], **Ahmed M. Naglah** [b,c,*]

[a] *Department of Chemistry, University College in Al-Qunfudhah, Umm Al-Qura University, Makkah 21955, Saudi Arabia*
[b] *Department of Pharmaceutical Chemistry, Drug Exploration & Development Chair (DEDC), College of Pharmacy, King Saud University, Riyadh 11451, Saudi Arabia*
[c] *Peptide Chemistry Department, Chemical Industries Research Division, National Research Centre, 12622-Dokki, Cairo, Egypt*

Received 3 October 2021; accepted 2 December 2021
Available online 9 December 2021

**KEYWORDS**

$Fe_2O_3$ nanoparticles;
Methylene blue dye;
Photocatalytic degradation;
L-lysine;
L-serine

**Abstract** In this work, $Fe_2O_3$ nanoparticles, abbreviated as OL and OS, were facilely synthesized by the combustion procedure using L-lysine and L-serine as organic fuels, respectively. Also, the OL and OS samples were identified using different instruments such as Raman spectrometer, FT-IR spectrophotometer, UV–Vis spectrophotometer, XRD, HR-TEM, BET surface area, and FE-SEM. The XRD confirmed that the mean grain size of OL and OS samples is 42.23 and 33.16 nm, respectively. The HR-TEM images confirmed that irregular, hexagonal, and spherical shapes, have an average diameter of 39.13 and 34.28 nm, were observed in the OL and OS samples, respectively. The BET surface area of the OL and OS samples is 16.20 and 28.34 $m^2/g$, respectively. Additionally, the OL and OS samples were accomplished for the photocatalytic degradation of methylene blue dye in the absence and presence of hydrogen peroxide. The % degradation of 45 mL of 25 mg/L of methylene blue dye in the case of using OL and OS samples in the absence of hydrogen peroxide is 55.23 and 63.64 % after 120 min, respectively. Also, in the presence of hydrogen peroxide, the % degradation in the case of using OL and OS samples is 100 % after 35 and 25 min, respectively.

## 1. Introduction

Rapid growth in industrial activities in the past decades has resulted in the continuous discharge of heavy metals and toxic organic pollutants into water bodies (Pandey et al., 2020; Pandey et al., 2020; Pandey et al., 2020). Organic dyes are essential in a lot of industries and they were worldwide

---

[*] Corresponding author at: Department of Pharmaceutical Chemistry, Drug Exploration & Development Chair (DEDC), College of Pharmacy, King Saud University, Riyadh 11451, Saudi Arabia.
E-mail address: anaglah@ksu.edu.sa (A.M. Naglah).

Peer review under responsibility of King Saud University.

Production and hosting by Elsevier

https://doi.org/10.1016/j.arabjc.2021.103613

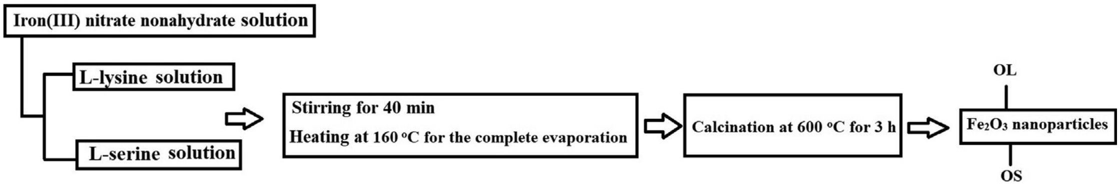

**Scheme 1** Practical steps for the synthesis of $Fe_2O_3$ nanoparticles.

produced at an undeniable degree (i.e., 7 × $10^5$ tones) (Aruna et al., 2021; Khan et al., 2021; Mishra et al., 2021). Excessive use of organic dyes led to the presence of 10–20 % of the dye components in the wastewater (Senguttuvan et al., 2021; Saya et al., 2021). The direct discharge of wastewater containing a lot of organic dyes is harmful to soil fertility, microorganisms, and aquatic organisms (Hasanpour and Hatami, 2020; Wazir et al., 2020). Methylene blue dye is a cationic thiazine dye that has widespread applications such as colorants, treating fish's fungal infection, inhibiting nitrification as well as medicinal aids. Harmful influences of acute exposure to methylene blue dye result in health ailments such as nausea, necrosis, vomiting, diarrhea, and eye irritation. Consequently, the removal of methylene blue dye from the wastewater stream is of important concern (Chandarana et al., 2021). To remove organic dyes, several techniques such as ion exchange, adsorption, ultrafiltration, photocatalytic degradation, biological treatment, reverse osmosis, chlorination, and flocculation are used (Islam et al., 2019; Badvi and Javanbakht, 2021; Hu et al., 2021; Benkhaya et al., 2021; Chowdhury et al., 2020; Feng et al., 2021; Kumaravel et al., 2021; Wang et al., 2018). However, these techniques, except for photocatalytic degradation, are slower in removing strong organic dyes. The photocatalytic degradation method is an effective approach that degrades organic dyes from wastewater. It is depending on exciting the electrons in the valence band and transferring them into the conduction band via absorbing photons from light sources such as UV irradiations. The holes (which were formed at valence band) and electrons (which were formed at conduction band) are involved in several steps to produce hydroxyl free radicals that can efficiently degrade a lot of organic dyes (Ali et al., 2020; Brites et al., 2011; Govindhan and Pragathiswaran, 2019; Khan et al., 2016; Mahmoodi, 2014). Various catalysts were utilized for the degradation of organic dyes such as g-$C_3N_4$/$TiO_2$/bentonite, $SnO_2$, Pd/$CeO_2$, $SrTiO_3$, $Fe_2O_3$, ZnS, ZnSe/ZnO, $TiO_2$, $Ag_3PO_4$/AgBr, SnSe/$LaNdZr_2O_7$, $CoWO_4$, and CdS/CdO (Mishra et al., 2018; E. G.D.R. S., G.K. A., S. S., R. R., T.S. Silambarasan, S.L. I., Y. Chen, , 2020; Channei et al., 2019; Gao et al., 2018; Ali and Mansor, 2020; Ehsan et al., 2018; Pragathiswaran et al., 2021; Wang et al., 2014; Karamat et al., 2019; Taneja et al., 2018; Saha et al., 2020). Mechouche et al. reported that 0.05 g of silver nanoparticles displayed a photocatalytic decolorization potential of 71.3 % for 250 mL of 20 mg/L of methylene blue dye using sunlight irradiation within 6 h, while only 11.25 % of the methylene blue dye was degraded using UV irradiation (Mechouche et al., 2021). Almehizia et al. reported that 0.20 g of zinc oxide nanoparticles displayed a photocatalytic decolorization potential of 54.69 % for 50 mL of 10 mg/L of methylene blue dye using UV irradiation within 90 min (Almehizia et al., 2021). Stanley et al. reported that 0.10 g of Ag-ZnO nanocomposite displayed a photocatalytic decolorization potential of 98.50 % for 100 mL of 10 mg/L of methylene blue dye using sunlight irradiation within 30 min (S. R., J.A. Jebasingh, M.V. S., P.K. Stanley, P. Ponmani, M.E. Shekinah, J. Vasanthi, , 231 (2021)). Chakraborty et al. reported that 0.002 g of $Ag_2O$-ZnO composite displayed a photocatalytic decolorization potential of 97.00 % for 10 mL of 20 mg/L of methylene blue dye using UV irradiation within 30 min (Chakraborty et al., 2021). Nanomaterials have a wide range of applications in biosensor, water remediation, energy etc. (Kim et al., 2021; Arshad et al., 2021; Sabir et al., 2021; Sargazi et al., 2021). Recently, $Fe_2O_3$ nanoparticles exhibit better potential in the degradation of organic dyes under light irradiation due to their resistance to corrosion, non-toxicity, and high efficiency (Hegazey et al., 2019; Alharbi and Abdelrahman, 2020; Abdelrahman et al., 2019; Jayaprakash et al., 2021). Hydrothermal treatment, microwave-assisted with ultrasound, co-precipitation, thermal decomposition, electrospinning, and combustion methods are the synthetic procedures for the production of $Fe_2O_3$ nanoparticles (Pu et al., 2014; Yang et al., 2016; Lassoued et al., 2018; Liang et al., 2017; Davar et al., 2016; Supattarasakda et al., 2013; Yang et al., 2018; Wang et al., 2017). The combustion technique was operated for the synthesis of different nanoparticles, specially $Fe_2O_3$, due to its low heat consumption, low cost, and simplicity. In this regard, various organic fuels such as glutamine, L-arginine, L-valine, L-alanine, urea, and citric acid have been used for the synthesis of $Fe_2O_3$ nanoparticles (Hegazey et al., 2019; Alharbi and Abdelrahman, 2020; Abdelrahman et al., 2019). It is known that organic fuels vary in their reducing power and the quantity of evolved gases. Consequently, the fuels influence the characteristics of the final nanoparticles such as morphology, crystallite size, and photocatalytic efficiency. To the best of our information, there are no scientific papers on the synthesis of $Fe_2O_3$ nanoparticles operating L-lysine and L-serine fuels. So, our team aims to synthesize $Fe_2O_3$ nanoparticles using the previous promising fuels for the first time. Also, our team aims to use the synthesized $Fe_2O_3$ nanoparticles as photocatalysts to degrade the methylene blue dye with high efficiency compared to other photocatalysts found in the literature.

**(A)**

$$14\ Fe(NO_3)_3.9H_2O + C_6H_{14}N_2O_2 \rightarrow 7\ Fe_2O_3 + 44\ NO_2 + 6\ CO_2 + 16\ H_2O$$

**(B)**

$$34\ Fe(NO_3)_3.9H_2O + 6\ C_3H_7NO_3 \rightarrow 17\ Fe_2O_3 + 108\ NO_2 + 18\ CO_2 + 30\ H_2O$$

**Scheme 2** Proposed mechanism for the synthesis of $Fe_2O_3$ nanoparticles using L-lysine (A) and L-serine (B).

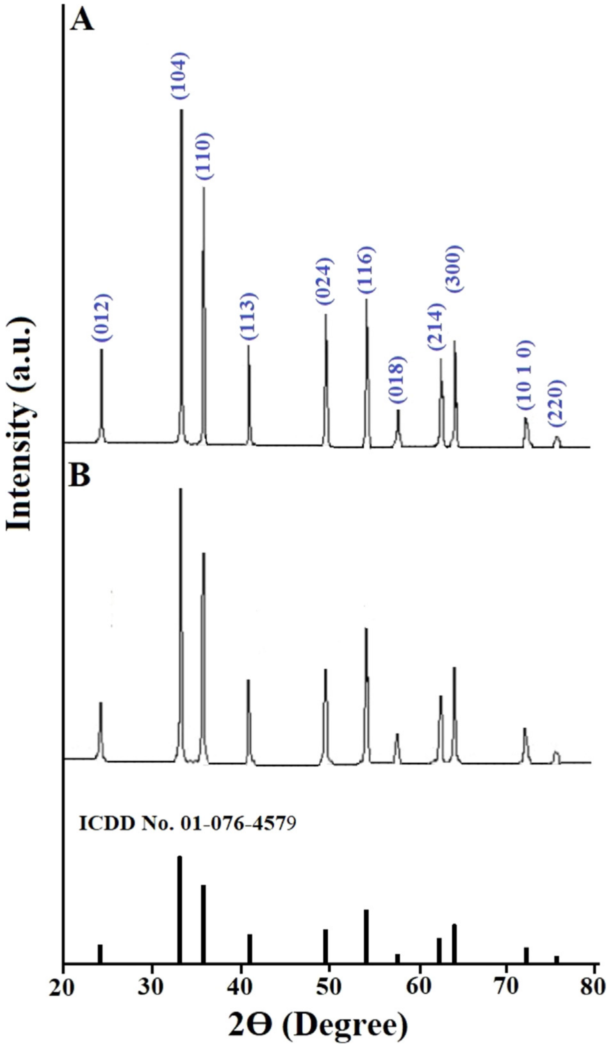

**Fig. 1** XRD patterns of the OL (A) and OS (B) samples.

## 2. Experimental

### 2.1. Chemicals

Iron(III) nitrate nonahydrate ($Fe(NO_3)_3 \cdot 9H_2O$), methylene blue dye ($C_{16}H_{18}ClN_3S$), hydrogen peroxide ($H_2O_2$), L-lysine ($C_6H_{14}N_2O_2$), L-serine ($C_3H_7NO_3$), isopropyl alcohol ($C_3H_8O$), disodium ethylenediaminetetraacetate dihydrate ($C_{10}H_{14}N_2Na_2O_8 \cdot 2H_2O$), and ascorbic acid ($C_6H_8O_6$) were of analytical grade and purchased from Sigma-Aldrich (Purity = 99.99 %) and used as received without any refining.

### 2.2. Synthesis of $Fe_2O_3$ nanoparticles

Firstly, 8.00 g (19.80 mmoles) of iron(III) nitrate nonahydrate was dissolved in 80 mL of distilled water. After that, 80 mL aqueous solution of L-lysine (0.20 g, 1.37 mmoles) or L-serine (0.37 g, 3.52 mmoles) were added to the previous iron solution drop by drop with constant stirring for 40 min utilizing a magnetic stirrer at 28 °C. Besides, the temperature of the utilized magnetic stirrer was raised to 160 °C for the complete evaporation of the mixture. Additionally, the formed powder was calcined at 600 °C for 3 h to produce $Fe_2O_3$ nanoparticles. The samples, which were produced using L-lysine and L-serine, were abbreviated as OL and OS, respectively. The above-mentioned practical steps have been summarized in Scheme 1.

### 2.3. Photocatalytic activity

The photocatalytic degradation of methylene blue dye using OL or OS nanoparticles in the presence of UV irradiations was accomplished as the following; 0.15 g of OL or OS sample was mixed with 45 mL of 25 mg/L of methylene blue dye solution then stirred for 2 h in a dark place to ensure adsorption/desorption equilibrium. Additionally, the illumination of methylene blue dye by UV irradiations in the presence of OL or OS nanoparticles was examined for different time intervals utilizing xenon arc lamp of 250 W and 365 nm (Toshiba, SHLS-002). Furthermore, after recovering the OL or OS nanoparticles using the centrifugation procedure, the absorption and concentration of the methylene blue dye solution were determined at 663 nm using a Shimadzu 2600 UV–Vis spectrophotometer. Moreover, % degradation (% P) of methylene blue dye was calculated using Eq. (1).

$$\%P = (X_o - X_t)100/X_o \quad (1)$$

where, $X_o$ (mg/L) is the concentration of methylene blue dye at equilibrium. Also, $X_t$ (mg/L) is the concentration of methylene blue dye at irradiation time t. To recognize the active kinds produced in the photocatalytic degradation of methylene blue dye, the scavengers including 5 M ascorbic acid, isopropyl alcohol, and disodium ethylenediaminetetraacetate (EDTA) were mixed with the solution of methylene blue dye then the photocatalytic degradation was carried as the same as that illustrated above.

### 2.4. Characterization

FT-IR spectra of the OL and OS nanoparticles were obtained by the KBr pellets method in the range 4000–400 $cm^{-1}$ utilizing a Bruker (Equinox 55) spectrophotometer (Riga, Latvia). Raman spectra of the OL and OS nanoparticles were obtained by a Thermo Scientific DXR spectrometer (Riga, Latvia) at an excitation wavelength of 532 nm in the range 2000–100 $cm^{-1}$. The morphology of the OL and OS nanoparticles was examined utilizing a field emission scanning electron microscopy (FE-SEM, SU8000, HITACHI, Chiyoda, Tokyo, Japan) and high-resolution transmission electron microscopy (JEOL 2100, Akishima, Tokyo, Japan). The XRD patterns of the OL and OS nanoparticles were obtained utilizing a Bruker (Cu $K_\alpha$ = 0.154 nm) X-ray diffractometer (Malvern, United Kingdom). The optical properties of the OL and OS nanoparticles were obtained utilizing a Shimadzu 2600 UV–Vis spectrophotometer (Kyoto, Japan). The surface texturing properties such as BET surface area, mean pore radius, and total pore volume of the OL and OS samples were measured from $N_2$ adsorption isotherms at 77 K utilizing a Quantachrome apparatus (Boynton Beach, United States) after sample out-gassing at 473 K for 12 h.

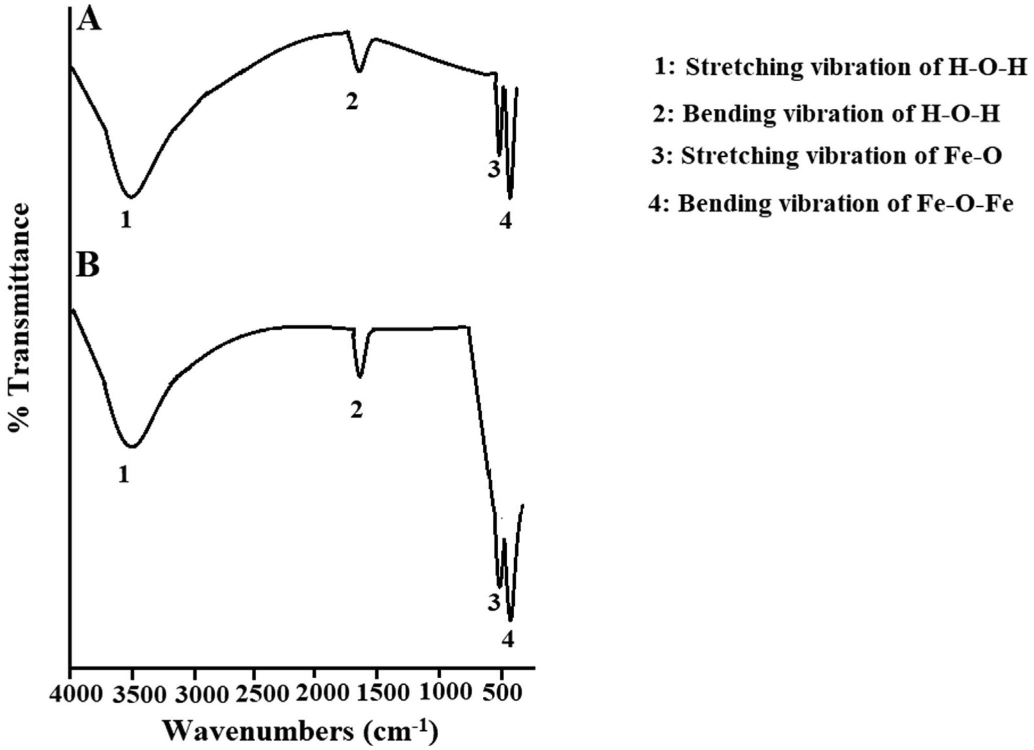

**Fig. 2** FT-IR spectra of the OL (A) and OS (B) samples.

## 3. Results and discussion

### 3.1. Characterization of $Fe_2O_3$ nanoparticles

Scheme 2A–B displays the mechanism of combustion procedure for the synthesis of OL and OS samples using L-lysine and L-serine, respectively. Furthermore, Fig. 1A–B displays the XRD patterns of the OL and OS samples which were synthesized using L-lysine and L-serine fuels, respectively. The data confirmed the existence of eleven typical peaks for hematite (Rhombohedral $Fe_2O_3$) (ICDD No. 01–076-4579) at 2θ = 24.23°, 33.25°, 35.77°, 40.96°, 49.58°, 54.18°, 57.76°, 62.55°, 64.09°, 72.05°, and 75.57° signifying (0 1 2), (1 0 4), (1 1 0), (1 1 3), (0 2 4), (1 1 6), (0 1 8), (2 1 4), (3 0 0), (10 10), and (2 2 0) lattice planes, respectively (Hegazey et al., 2019). Additionally, the grain size of the OL and OS samples, which can be gotten applying the Scherrer equation, is 42.23 and 33.16 nm, respec-

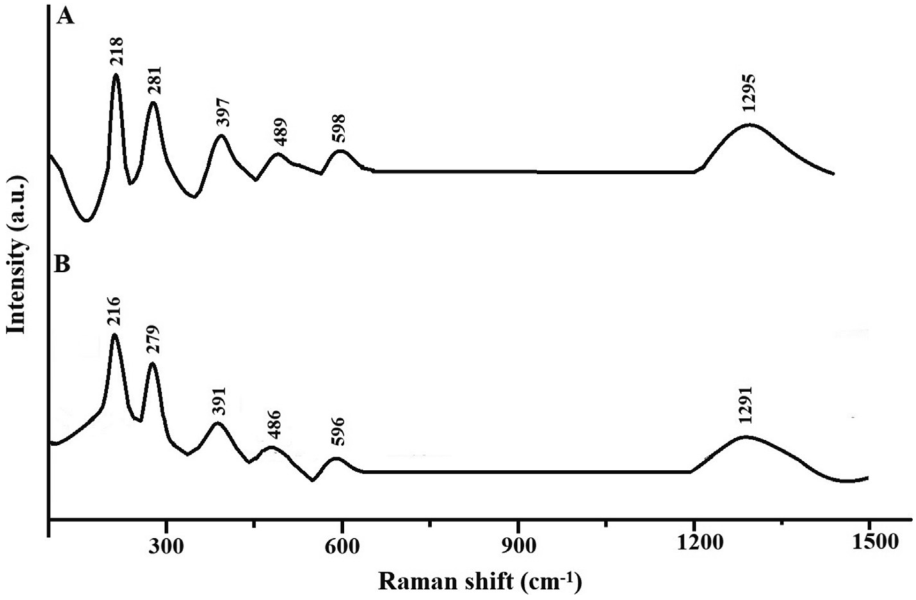

**Fig. 3** Raman spectra of the OL (A) and OS (B) samples.

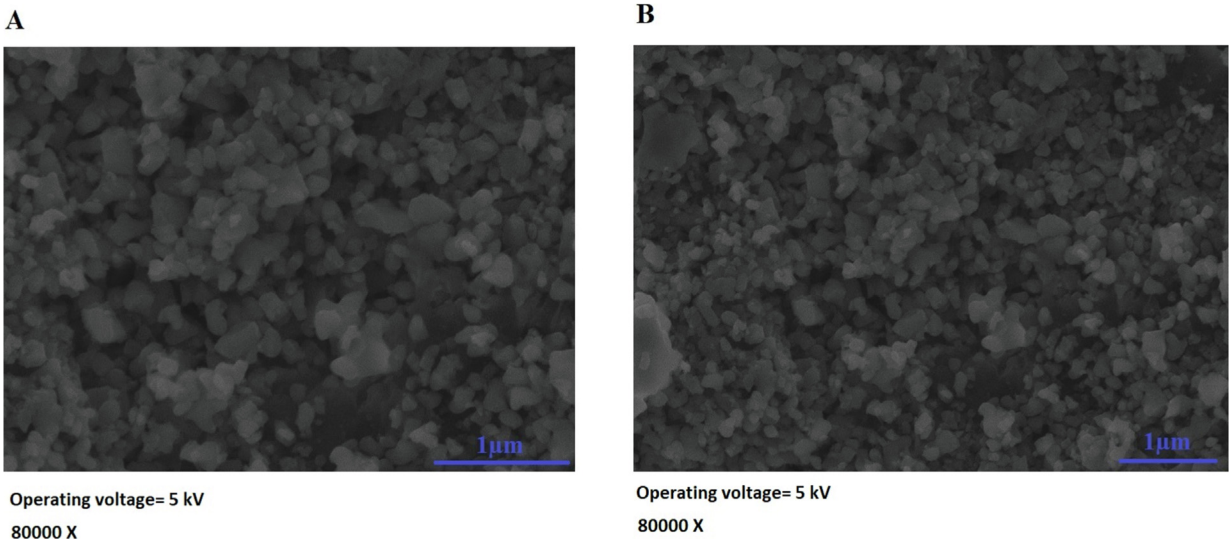

Operating voltage= 5 kV
80000 X

Operating voltage= 5 kV
80000 X

**Fig. 4** FE-SEM images of the OL (A) and OS (B) samples.

tively. Fig. 2A–B displays the FT-IR spectra of the OL and OS samples, respectively. The existence of FT-IR bands at about 3500 and 1600 $cm^{-1}$ signifies the stretching and bending vibration of H—O—H of adsorbed water, respectively. Additionally, the existence of FT-IR bands at about 430 and 518 $cm^{-1}$ signifies the vibrations of the Fe—O bond (Hegazey et al., 2019). Raman spectroscopy is a significant non-destructive tool to investigate the chemical and structural composition of a wide range of materials and has been regarded as the appropriate technique for characterization of nanosized substances since it allows to identify slights vibrations of nanomaterials. Fig. 3A–B displays the Raman spectra of the OL and OS samples, respectively. Additionally, the Raman peaks exist as expected for hematite. Consequently, the peaks, which were observed at (218 and 489 $cm^{-1}$) or (216 and 486 $cm^{-1}$), in the case of OL and OS samples, are attributed to two $A_{1g}$ symmetry modes, respectively. Moreover, the peaks, which were observed at (281, 397, and 598 $cm^{-1}$) or (279, 391, and 596 $cm^{-1}$), in the case of OL and OS samples, are attributed to $E_g$ symmetry modes, respectively. Furthermore, the peaks, which were observed at 1295 and 1291 $cm^{-1}$, in the case of OL and OS samples, are attributed to a second harmonic vibration, respectively (De Faria et al., 1997; Fei et al., 2013; Su et al., 2011; Xu et al., 2009; Dong et al, 2017; Al-Wasidi, 2021; Kotp, 2021; Kotp, 2019; El-Aassar et al., 2017; Shawky et al., 2020). Fig. 4A–B displays the FE-SEM images of the OL and OS samples, respectively. The results confirmed that spherical shapes have an average size of 201.20 and 148.67 nm, were observed in the OL and OS samples, respectively. Fig. 5A–B displays the HR-TEM images of the OL and OS nanoparticles, respectively. The results confirmed that irregular, hexagonal, and spherical shapes, have an average

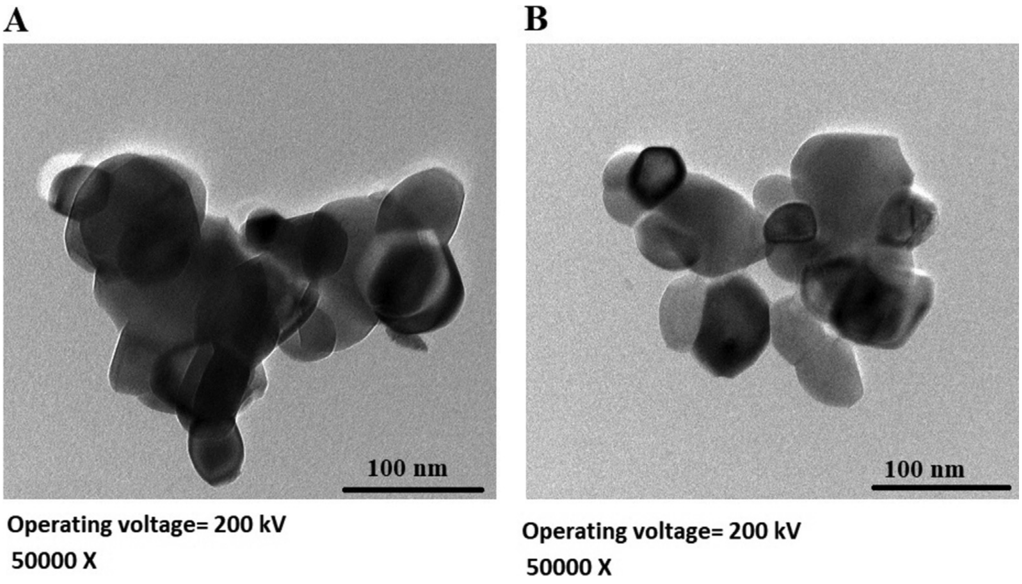

Operating voltage= 200 kV
50000 X

Operating voltage= 200 kV
50000 X

**Fig. 5** HR-TEM images of the OL (A) and OS (B) samples.

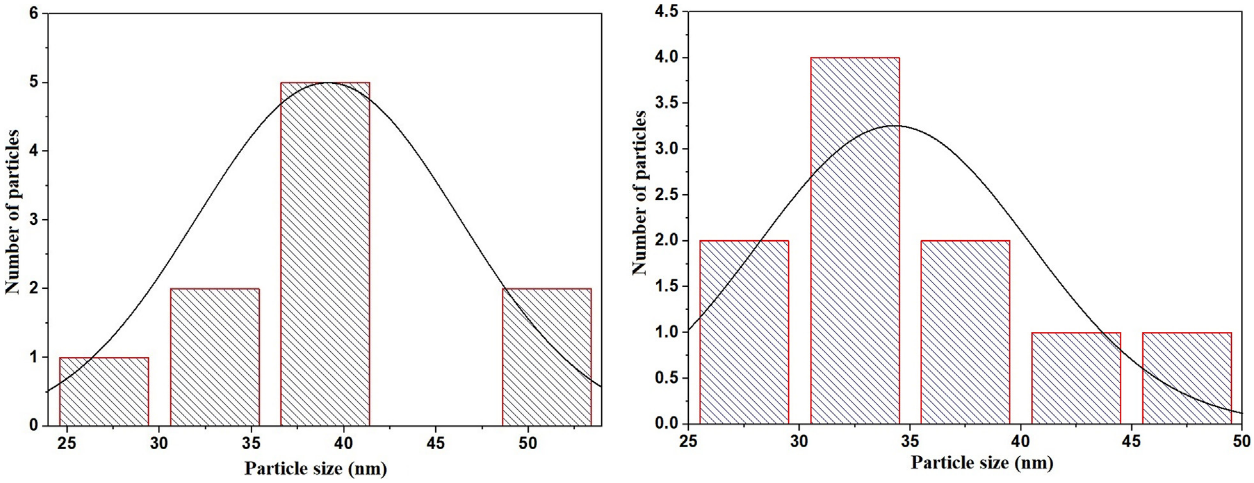

**Fig. 6** HR-TEM histogram of the OL (A) and OS (B) samples.

diameter of 39.13 and 34.28 nm, were observed in the OL and OS samples as clarified from TEM histograms as shown in Fig. 6A–B, respectively. The estimated diameters using HR-TEM and XRD were almost identical. The values of the energy gap ($E_g$) can be obtained from Tauc's equation as described in Eq. (2) (Hegazey et al., 2019).

$$(Yh\upsilon)^J = C(h\upsilon - E_g) \quad (2)$$

where, Y is the absorption coefficient whereas h is the Planck constant. Also, C is a substance constant whereas υ is the frequency of light. Moreover, J is an integer depending on the kind of electronic transitions. Furthermore, J equals 2.00 and 0.50 in the case of direct and indirect transitions, respectively. Fig. 7A–B displays the plot of $(Yh\upsilon)^2$ versus hυ for the OL and OS samples, respectively. Accordingly, this confirmed that the kind of transitions in OL or OS samples is direct. The direct energy gap is estimated from the extrapolation of the straight line so that $(Yh\upsilon)^2$ equals 0. The value of the energy gap ($E_g$) for the OL and OS samples is 0.97 and 1.35 eV, respectively. The difference in the energy gap ($E_g$) for the OL and OS samples is large because of the great difference in grain size.

The elemental composition of the OL and OS samples was analyzed by energy dispersive spectroscopy as shown in Fig. 8A–B, respectively. The results showed the presence of Fe and O peaks which indicating the absence of impurities. The Au peaks were because of gold coating done on the samples before SEM measurement. % Fe in the OL and OS samples is 60.85 and 60.50 %, respectively. % O in the OL and OS samples is 39.15 and 39.50 %, respectively.

The BET nitrogen adsorption-desorption isotherms of the OL and OS samples are given in Fig. 9A–B, respectively. The surface textural results are displayed in Table 1. The obtained isotherms belong to type IV. The OS sample gives the highest surface area value and hence possesses the higher photocatalytic activity because it has the highest active sites.

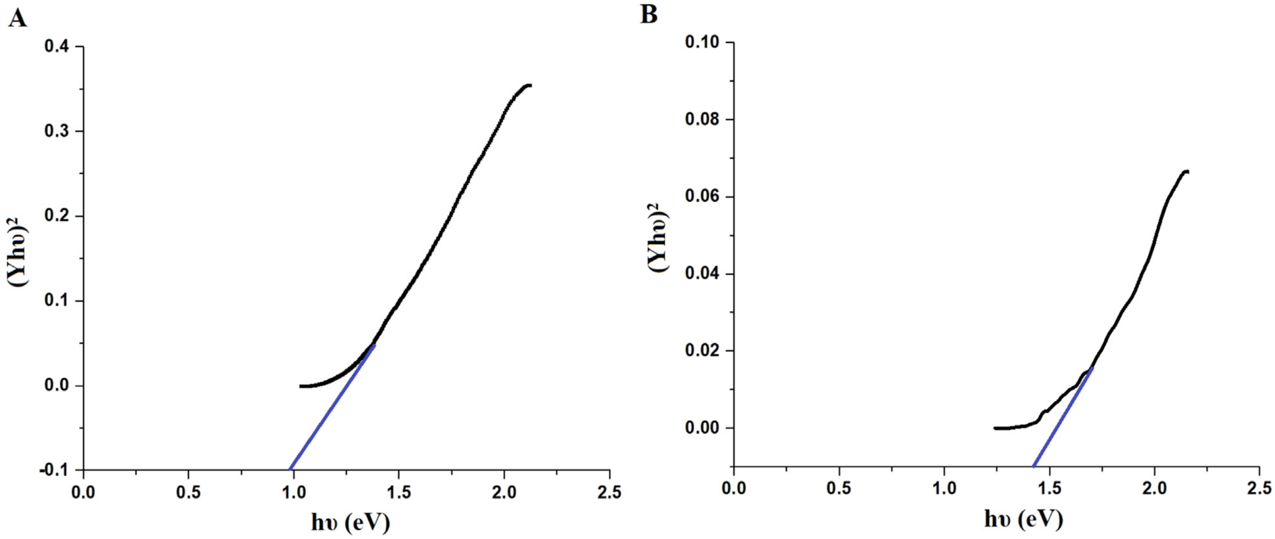

**Fig. 7** Energy gap of the OL (A) and OS (B) samples.

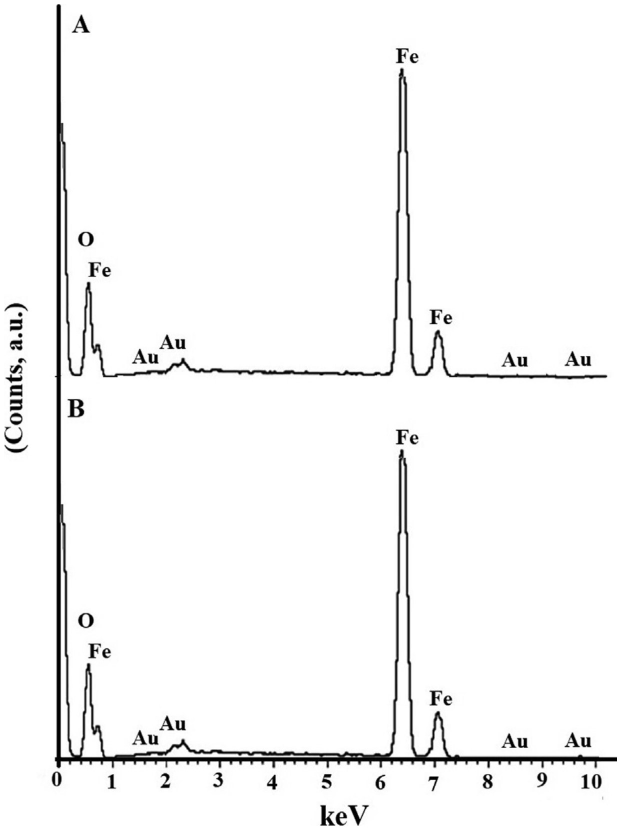

**Fig. 8** EDS of the OL (A) and OS (B) samples.

### 3.2. Photocatalytic degradation of methylene blue dye

Fig. 10A–B displays the plot of % P versus UV irradiation time utilizing the OL and OS samples in the absence of hydrogen peroxide, respectively. Also, Fig. 11A–B displays the plot of % % P versus UV irradiation time utilizing the OL and OS samples in the presence of hydrogen peroxide, respectively. The data show that the % P of methylene blue dye in the case of using OL and OS samples in the absence of hydrogen peroxide is 55.23 and 63.64 % after 120 min, respectively. Also, the % P of methylene blue dye in the case of using the OL and OS samples in the presence of hydrogen peroxide is 100 % after 35 and 25 min, respectively. Furthermore, the photocatalytic degradation of methylene blue dye was investigated using the first-order kinetic model as clarified in Eq. (3) (Hegazey et al., 2019).

$$\ln(X_o/X_t) = CPt \tag{3}$$

where, $C_P$ (1/min) represents the rate constant of the first-order kinetic model. Fig. 12A–B represents the plot of ln ($X_o/X_t$) versus UV irradiation time in the case of using the OL and OS samples in the absence of hydrogen peroxide, respectively. Also, Fig. 13A–B represents the plot of ln ($X_o/X_t$) versus UV irradiation time in the case of using the OL and OS samples in the presence of hydrogen peroxide, respectively. The data display that the photocatalytic degradation of methylene blue dye matched well with the first-order kinetic model. Besides, the correlation coefficients and constants of the first order in the case of using the OL and OS samples were tabulated in Table 2. Hence, the reaction rate is linearly dependent on the concentration of only one reactant i.e. methylene blue dye. In other words, a first-order reaction is a chemical reaction in which the rate varies based on the changes in the concentration of only one of the reactants i.e. methylene blue dye. Cp in the case of the presence of hydrogen peroxide is more than that in the absence of hydrogen peroxide because % P in the presence of hydrogen peroxide is more than that in the absence of hydrogen peroxide. Hydrogen peroxide when exposed to UV light produces more hydroxyl free radicals and thus the % P increases.

In the case of the heterogeneous photocatalysis process, some kinds of photoinduced reactive forms are generated, including oxygen anion radicals ($O_2^{\cdot-}$) and hydroxyl radicals ($OH^{\cdot}$), as well as the holes ($h^+$) and electrons ($e^-$) that can be responsible for the oxidation of the organic dye (Al-Wasidi et al., 2021). To investigate what kind of radicals plays the main role in the degradation of methylene blue dye, the inhibitors of hydroxyl radicals, holes, oxygen anion radicals,

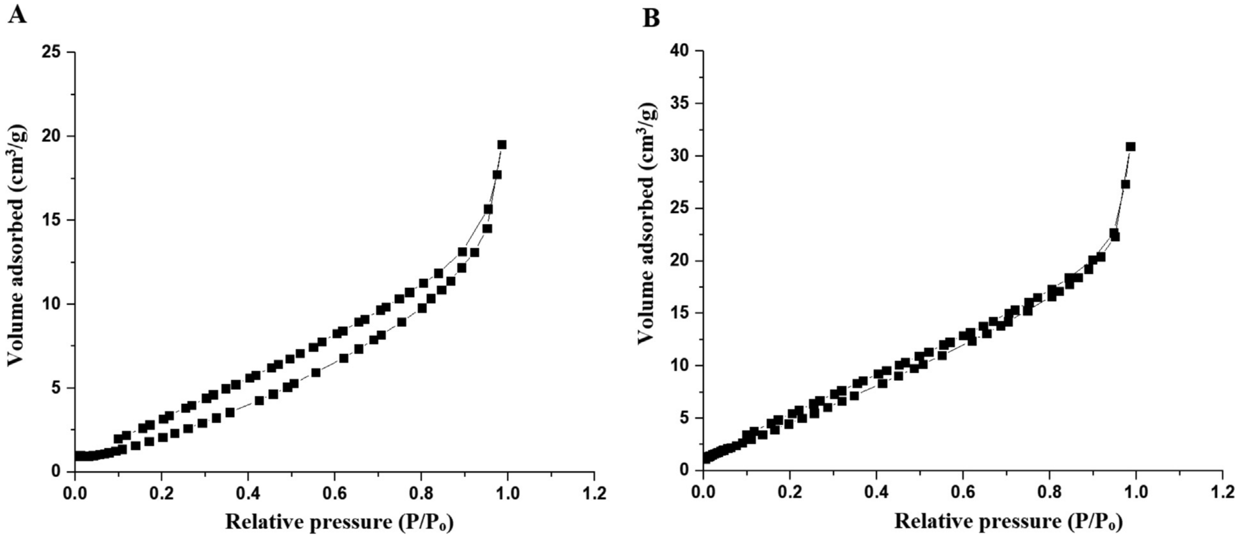

**Fig. 9** The BET nitrogen adsorption-desorption isotherms of the OL (A) and OS (B) samples.

**Table 1** Surface textures of the OL and OS samples.

| Sample | BET surface area ($m^2/g$) | Total pore volume ($cm^3/g$) | Mean pore radius ($A^o$) |
|---|---|---|---|
| OL | 16.20 | 3.12 E-02 | 40.74 |
| OS | 28.34 | 4.60 E-02 | 13.82 |

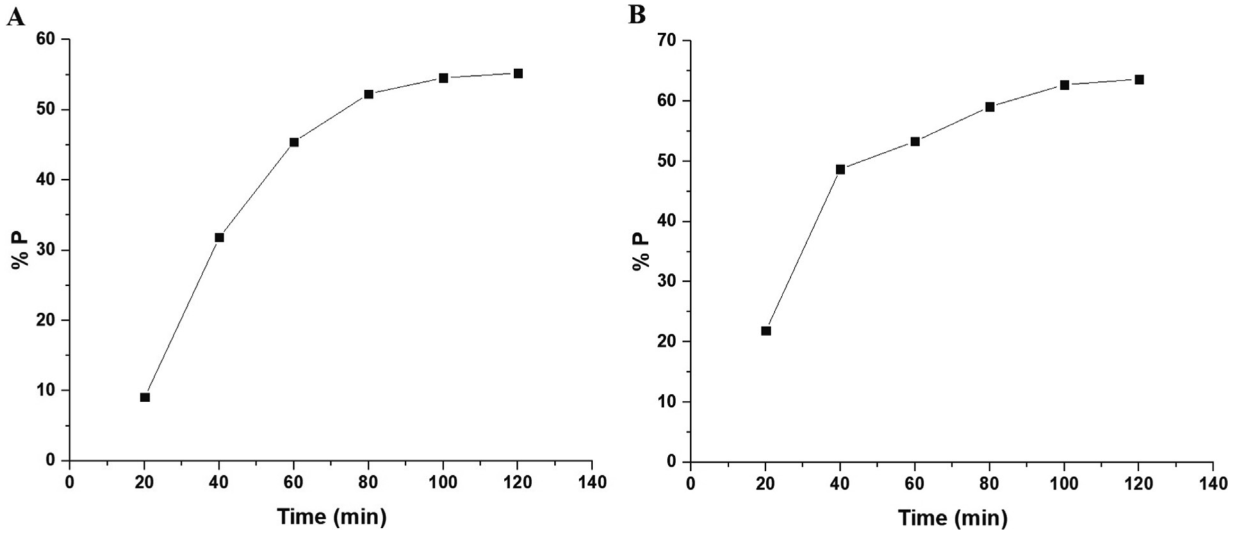

**Fig. 10** The plot of % P versus irradiation time in the absence of hydrogen peroxide in the case of the OL (A) and OS (B) samples.

isopropyl alcohol, disodium ethylenediaminetetraacetate dihydrate, and ascorbic acid were utilized. Fig. 14 demonstrated that the presence of disodium ethylenediaminetetraacetate dihydrate extensively reduces the % P of the methylene blue dye, confirming that holes play a basic role in the degradation process. Also, in the case of ascorbic acid, a slight decrease in the % P of the methylene blue dye is detected, confirming a minor concentration of oxygen anion radicals. Besides, the degradation of the methylene blue dye was reduced in the presence of isopropyl alcohol, confirming that the hydroxyl radicals play a basic role in the degradation process of the methylene blue dye. Consequently, holes and hydroxyl radicals are the two principal active kinds in the degradation of methylene blue dye (Al-Wasidi et al., 2021).

The synthesized OL and OS samples were regenerated and reused for three succeeding batches. The results confirmed that % P of the methylene blue dye using the OL and OS samples was conserved with a minor decrease as shown in Table 3.

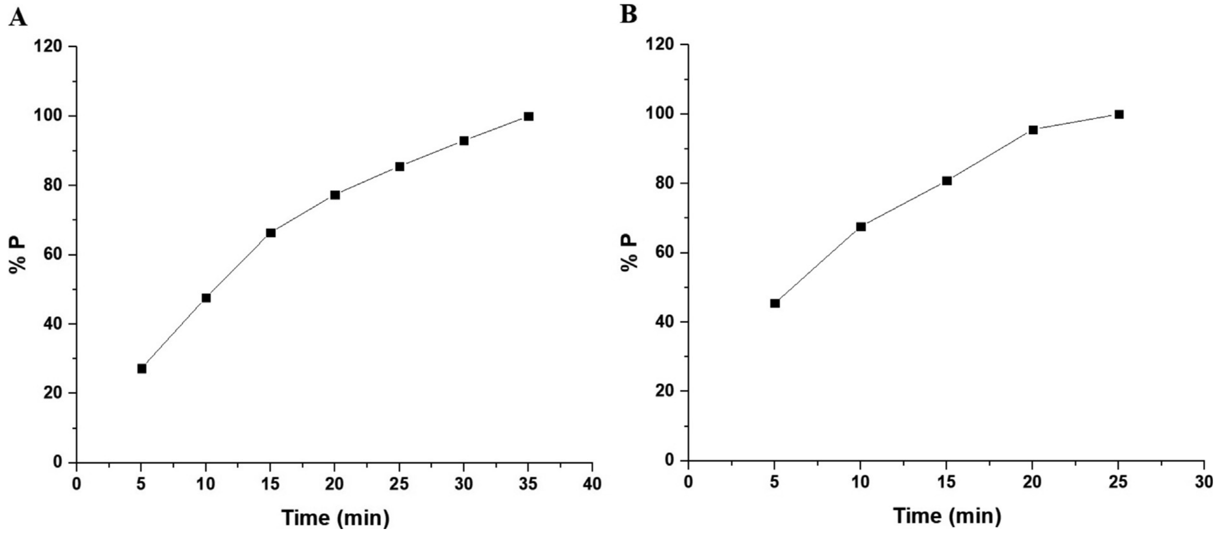

**Fig. 11** The plot of % P versus irradiation time in the presence of hydrogen peroxide in the case of the OL (A) and OS (B) samples.

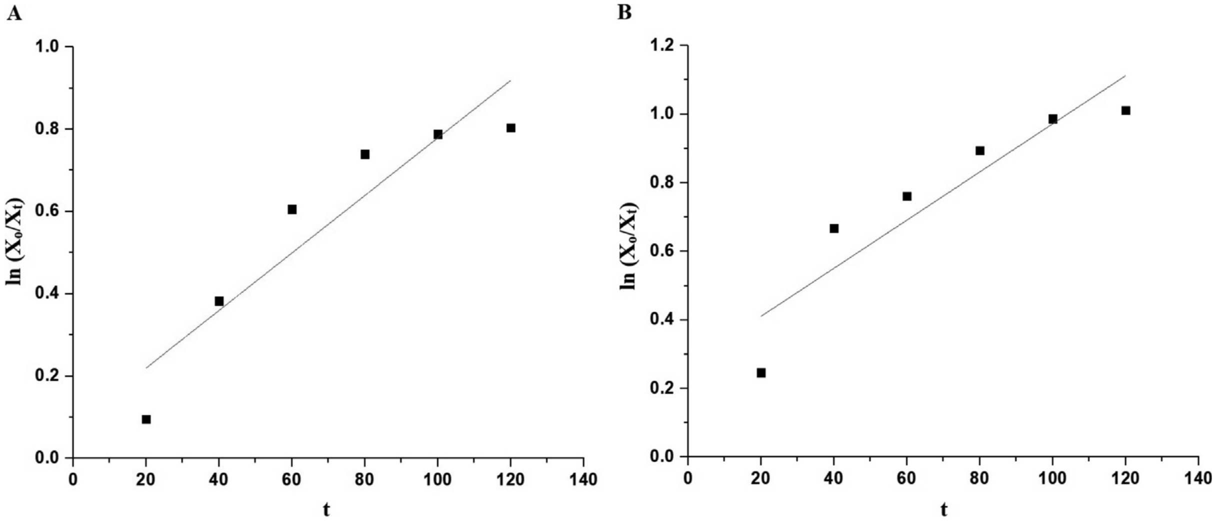

**Fig. 12** The plot of ln $(X_o/X_t)$ versus irradiation time in the absence of hydrogen peroxide in the case of the OL (A) and OS (B) samples.

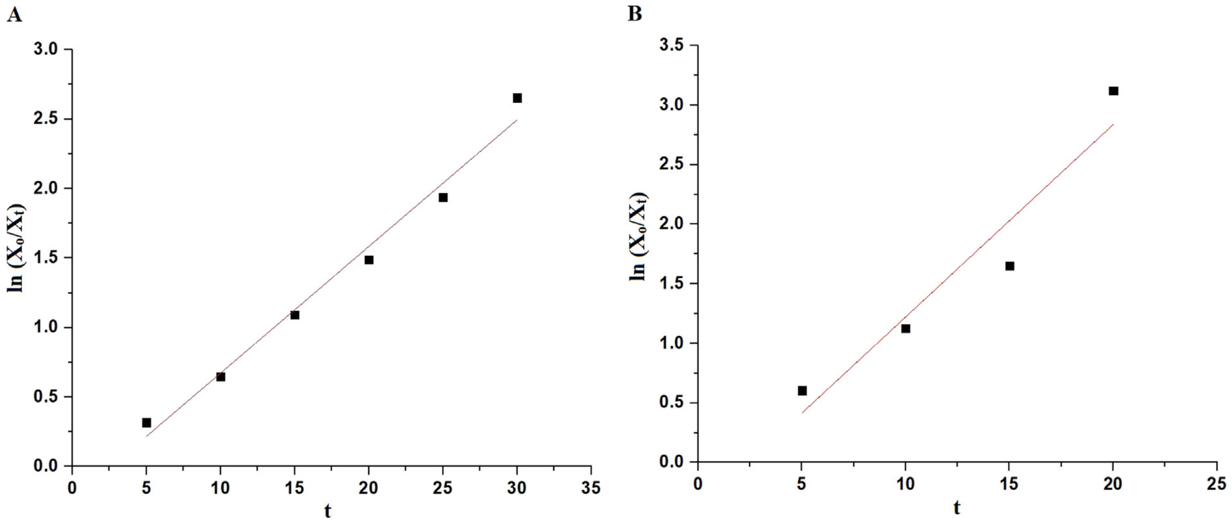

**Fig. 13** The plot of ln $(X_o/X_t)$ versus irradiation time in the presence of hydrogen peroxide in the case of the OL (A) and OS (B) samples.

Besides, to reutilize the OL and OS photocatalysts, the samples were carefully washed with hot distilled water after the end of the first batch, and an approximately equivalent amount was attained, which was reutilized for the following batches. We have carried the XRD for OL and OS samples after recycling experiments (figure omitted for brevity). We found that the positions and intensities of peaks did not change. Hence, the structure of the OL and OS samples is stable. Consequently, the OL and OS samples can be utilized many times without losing their effectiveness.

The proposed mechanism of the photocatalytic degradation of methylene blue dye in the presence of OL or OS samples and UV has been described in Scheme 3 (Hegazey et al., 2019). It is depending on exciting the electrons in the valence band and transferring them into the conduction band via absorbing photons from light sources such as UV irradiations. The holes

**Table 2** Kinetic constants for the methylene blue dye degradation using OL and OS samples.

| Sample | Parameters | |
|---|---|---|
| | $R^2$ | $C_P$ (1/min) |
| OL in the absence of $H_2O_2$ | 0.870 | 0.0069 |
| OL in the presence of $H_2O_2$ | 0.985 | 0.0910 |
| OS in the absence of $H_2O_2$ | 0.852 | 0.0070 |
| OS in the presence of $H_2O_2$ | 0.923 | 0.1614 |

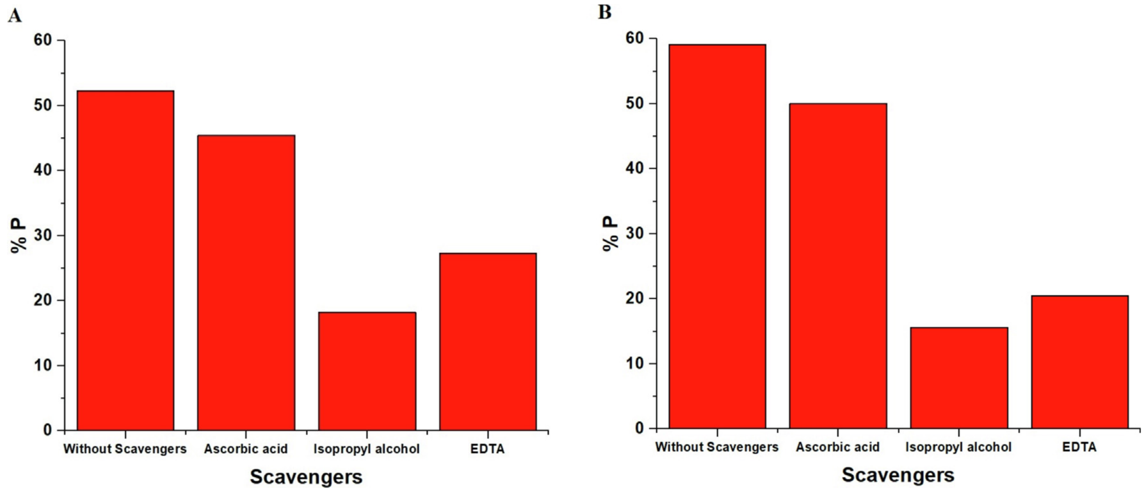

**Fig. 14** The effect of scavengers in the case of the OL (A) and OS (B) photocatalysts.

**Table 3** Recycling and reuse of OL and OS samples for photocatalytic degradation of methylene blue dye.

| Sample | % P after 1st batch | % P after 2nd batch | % P after 3rd batch |
|---|---|---|---|
| OL | 52.18 | 50.29 | 48.53 |
| OS | 58.30 | 56.06 | 55.27 |

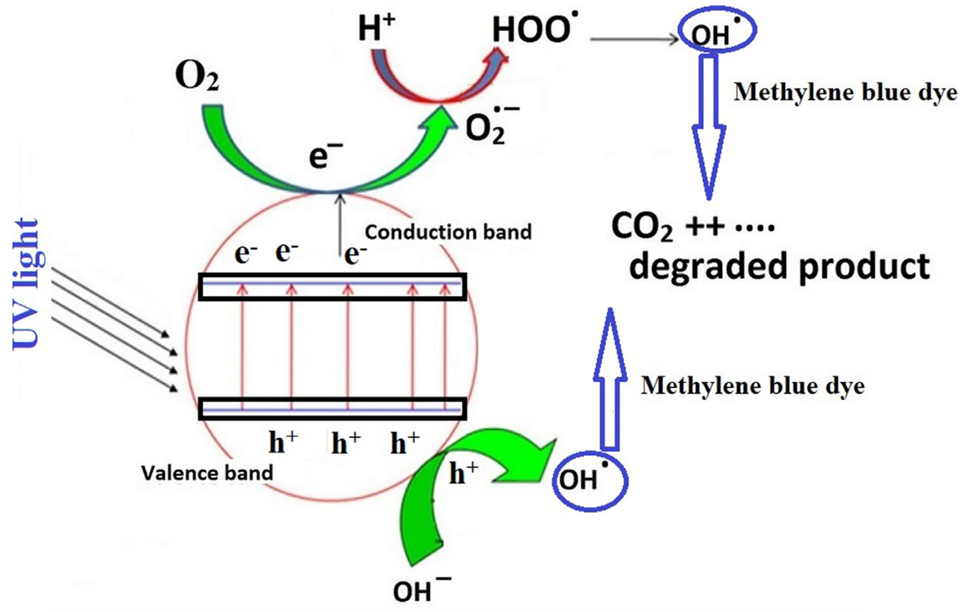

$Fe_2O_3 + UV \longrightarrow h^+_{VB} + e^-_{CB}$ $H_2O \longrightarrow H^+ + OH^-$

$h^+_{VB} + OH^- \longrightarrow OH^\bullet$ $e^-_{CB} + O_2 \longrightarrow O_2^{\bullet -}$

$O_2^{\bullet -} + H^+ \longrightarrow HOO^\bullet$ $2\,HOO^\bullet \longrightarrow H_2O_2 + O_2$

$H_2O_2 + UV \longrightarrow 2OH^\bullet$ $H_2O_2 + e^-_{CB} \longrightarrow OH^\bullet + OH^-$

**Scheme 3** Proposed mechanism for the degradation of methylene blue dye.

**Table 4** Comparative study between the % P of the OL or OS samples and that of other photocatalysts in the literature.

| Photocatalyst | | Methylene blue Dye | | % Degradation | | Ref |
|---|---|---|---|---|---|---|
| Name | W (g) | X(mg/L) | V(mL) | Value | Time (min) | |
| Co alloyed CdZnS | 0.03 | 25 | 25 | 83 | 100 | (Abdelrahman et al., 2019) |
| CuO | 0.1 | 10 | 50 | 96.18 | 360 | (Abdelrahman et al., 2019) |
| ZnO | 0.1 | 10 | 50 | 95 | 45 | (Dong et al., 2017) |
| Silver nanoparticles | 0.05 | 20 | 250 | 11.25 | 360 | (Mechouche et al., 2021) |
| $Ag_2O$-ZnO composite | 0.002 | 20 | 10 | 97.00 | 30 | (Chakraborty et al., 2021) |
| $Fe_2O_3$ (OL) | 0.15 | 25 | 45 | 100 | 35 | **This study** |
| $Fe_2O_3$ (OS) | 0.15 | 25 | 45 | 100 | 25 | **This study** |

V = Volume, X = Concentration, and W = Weight.

(which were formed at valence band) and electrons (which were formed at conduction band) are involved in several steps to produce hydroxyl free radicals that can efficiently degrade methylene blue dye. Table 4 displays a comparative study between the % P of the OL or OS samples and that of other photocatalysts in the literature such as Co alloyed CdZnS, CuO, silver nanoparticles, $Ag_2O$-ZnO composite, and ZnO for the degradation of methylene blue dye. The comparison confirmed that the OL and OS samples efficiently degrades the methylene blue dye.

## 4. Conclusions

The combustion approach was used for the facile synthesis of $Fe_2O_3$ nanoparticles, abbreviated as OL and OS, using L-lysine and L-serine as organic fuels, respectively. The mean grain size of the OL and OS samples is 42.23 and 33.16 nm, respectively. The BET surface area of the OL and OS samples is 16.20 and 28.34 m2/g, respectively. Also, the OL and OS samples were used for the photocatalytic degradation of methylene blue dye. The % degradation of 45 mL of 25 mg/L of methylene blue dye in the case of using the OL and OS samples in the absence of hydrogen peroxide is 55.23 and 63.64 % after 120 min, respectively. Besides, in the presence of hydrogen peroxide, the % degradation in the case of using the OL and OS samples is 100 % after 35 and 25 min, respectively. Moreover, holes and hydroxyl radicals are the two principal active kinds in the degradation of methylene blue dye.

## Declaration of Competing Interest

The authors declare that they have no known competing financial interests or personal relationships that could have appeared to influence the work reported in this paper.

## Acknowledgments

The authors are grateful to the Deanship of Scientific Research, King Saud University for funding through Vice Deanship of Scientific Research Chairs.

## References

Pandey, S., Do, J.Y., Kim, J., Kang, M., 2020. Fast and highly efficient catalytic degradation of dyes using κ-carrageenan stabilized silver nanoparticles nanocatalyst. Carbohydr. Polym. 230, 115597.

Pandey, S., Do, J.Y., Kim, J., Kang, M., 2020. Fast and highly efficient removal of dye from aqueous solution using natural locust bean gum based hydrogels as adsorbent. Int. J. Biol. Macromol. 143, 60–75.

Pandey, S., Fosso-Kankeu, E., Spiro, M.J., Waanders, F., Kumar, N., Ray, S.S., Kim, J., Kang, M., 2020. Equilibrium, kinetic, and thermodynamic studies of lead ion adsorption from mine wastewater onto MoS2-clinoptilolite composite. Mater. Today Chem. 18, 100376.

Aruna, N., Bagotia, A.K., Sharma, S., 2021. Kumar, A review on modified sugarcane bagasse biosorbent for removal of dyes. Chemosphere 268, 129309.

Khan, F.S.A., Mubarak, N.M., Tan, Y.H., Khalid, M., Karri, R.R., Walvekar, R., Abdullah, E.C., Nizamuddin, S., Mazari, S.A., 2021. A comprehensive review on magnetic carbon nanotubes and carbon nanotube-based buckypaper for removal of heavy metals and dyes. J. Hazard. Mater. 413, 125375.

Mishra, S., Cheng, L., Maiti, A., 2021. The utilization of agro-biomass/byproducts for effective bio-removal of dyes from dyeing wastewater: A comprehensive review. J. Environ. Chem. Eng. 9, 104901.

Senguttuvan, S., Senthilkumar, P., Janaki, V., Kamala-Kannan, S., 2021. Significance of conducting polyaniline based composites for the removal of dyes and heavy metals from aqueous solution and wastewaters - A review. Chemosphere 267, 129201.

Saya, L., Malik, V., Singh, A., Singh, S., Gambhir, G., Singh, W.R., Chandra, R., Hooda, S., 2021. Guar gum based nanocomposites: Role in water purification through efficient removal of dyes and metal ions. Carbohydr. Polym. 261, 117851.

Hasanpour, M., Hatami, M., 2020. Photocatalytic performance of aerogels for organic dyes removal from wastewaters: Review study. J. Mol. Liq. 309, 113094.

Wazir, M.B., Daud, M., Ali, F., Al-Harthi, M.A., 2020. Dendrimer assisted dye-removal: A critical review of adsorption and catalytic degradation for wastewater treatment. J. Mol. Liq. 315, 113775.

Chandarana, H., Senthil Kumar, P., Seenuvasan, M., Anil Kumar, M., 2021. Kinetics, equilibrium and thermodynamic investigations of methylene blue dye removal using Casuarina equisetifolia pines. Chemosphere 285.

Islam, M.A., Ali, I., Karim, S.M.A., Hossain Firoz, M.S., Chowdhury, A.N., Morton, D.W., Angove, M.J., 2019. Removal of dye from polluted water using novel nano manganese oxide-based materials. J. Water Process Eng. 32, 100911.

Badvi, K., Javanbakht, V., 2021. Enhanced photocatalytic degradation of dye contaminants with $TiO_2$ immobilized on ZSM-5 zeolite modified with nickel nanoparticles. J. Clean. Prod. 280, 124518.

Hu, Y., Yue, M., Yuan, F., Yang, L., Chen, C., Sun, D., 2021. Bio-inspired fabrication of highly permeable and anti-fouling ultrafiltration membranes based on bacterial cellulose for efficient removal of soluble dyes and insoluble oils. J. Memb. Sci. 621, 118982.

Benkhaya, S., Lgaz, H., Alrashdi, A.A., M'rabet, S., El Bachiri, A., Assouag, M., Chung, I.M., El Harfi, A., 2021. Upgrading the performances of polysulfone/polyetherimide ultrafiltration composite membranes for dyes removal: Experimental and molecular dynamics studies. J. Mol. Liq. 331, 115743.

Chowdhury, M.F., Khandaker, S., Sarker, F., Islam, A., Rahman, M. T., Awual, M.R., 2020. Current treatment technologies and mechanisms for removal of indigo carmine dyes from wastewater: A review. J. Mol. Liq. 318, 114061.

Feng, Q., Gao, B., Yue, Q., Guo, K., 2021. Flocculation performance of papermaking sludge-based flocculants in different dye wastewater treatment: Comparison with commercial lignin and coagulants. Chemosphere 262, 128416.

Kumaravel, S., Thiripuranthagan, S., Vembuli, T., Erusappan, E., Durai, M., Sureshkumar, T., Durai, M., 2021. Fabrication of mesoporous WO3-SBA-15 catalysts and enhanced photocatalytic degradation of harmful dyes. Optik (Stuttg) 235, 166599.

Wang, J., Zhang, T., Mei, Y., Pan, B., 2018. Treatment of reverse-osmosis concentrate of printing and dyeing wastewater by electro-oxidation process with controlled oxidation-reduction potential (ORP). Chemosphere 201, 621–626.

Ali, N., Said, A., Ali, F., Raziq, F., Ali, Z., Bilal, M., Reinert, L., Begum, T., Iqbal, H.M.N., 2020. Photocatalytic Degradation of Congo Red Dye from Aqueous Environment Using Cobalt Ferrite Nanostructures: Development, Characterization, and Photocatalytic Performance. Water. Air. Soil Pollut. 231, 50–60.

Brites, F.F., Santana, V.S., Fernandes-Machado, N.R.C., 2011. Effect of support on the photocatalytic degradation of textile effluents using $Nb_2O_5$ and ZnO: Photocatalytic degradation of textile dye. Top. Catal. 54, 264–269.

Govindhan, P., Pragathiswaran, C., 2019. Silver Nanoparticle Decorated on ZnO@SiO2 Nanocomposite and Application for Photocatalytic Dye Degradation of Methylene Blue. Natl. Acad. Sci. Lett. 42, 323–326.

Khan, R., Raj, S., Yun, J.H., Yu, Y.T., Lee, J.I., Lee, I.H., 2016. Facile preparation of ZnO nanosheets and its photocatalytic activity in the degradation of rhodamine B dye under UV irradiation. Electron. Mater. Lett. 12, 784–788.

Mahmoodi, N.M., 2014. Synthesis of magnetic carbon nanotube and photocatalytic dye degradation ability. Environ. Monit. Assess. 186, 5595–5604.

Mishra, A., Mehta, A., Kainth, S., Basu, S., 2018. Effect of g-$C_3N_4$ loading on $TiO_2$/Bentonite nanocomposites for efficient heterogeneous photocatalytic degradation of industrial dye under visible light. J. Alloys Compd. 764, 406–415.

Steplinpaulselvin, S., Rajaram, R., Silambarasan, T.S., Chen, Y., 2020. Survival assessment of simple food webs for dye wastewater after photocatalytic degradation using $SnO_2$/GO nanocomposites under sunlight irradiation. Sci. Total Environ. 721.

Channei, D., Nakaruk, A., Jannoey, P., Phanichphant, S., 2019. Preparation and characterization of Pd modified $CeO_2$ nanoparticles for photocatalytic degradation of dye. Solid State Sci. 87, 9–14.

Gao, H., Yang, H., Wang, S., 2018. Hydrothermal synthesis, growth mechanism, optical properties and photocatalytic activity of cubic $SrTiO_3$ particles for the degradation of cationic and anionic dyes. Optik (Stuttg) 175, 237–249.

Ali, H., Mansor, E.S., 2020. Co-sensitization of mesoporous ZnS with CdS and polyaniline for efficient photocatalytic degradation of anionic and cationic dyes. Colloids Interface Sci. Commun. 39, 100330.

Ehsan, M.F., Bashir, S., Hamid, S., Zia, A., Abbas, Y., Umbreen, K., Ashiq, M.N., Shah, A., 2018. One-pot facile synthesis of the ZnO/ZnSe heterostructures for efficient photocatalytic degradation of azo dye. Appl. Surf. Sci. 459, 194–200.

Pragathiswaran, C., Smitha, C., Mahin Abbubakkar, B., Govindhan, P., Anantha Krishnan, N., 2021. Synthesis and characterization of $TiO_2$/ZnO–Ag nanocomposite for photocatalytic degradation of dyes and anti-microbial activity. Mater. Today Proc. https://doi.org/10.1016/j.matpr.2020.12.664.

Wang, S., Li, D., Sun, C., Yang, S., Guan, Y., He, H., 2014. Highly efficient photocatalytic treatment of dye wastewater via visible-light-driven AgBr-$Ag_3PO_4$/MWCNTs. J. Mol. Catal. A Chem. 383–384, 128–136.

Karamat, N., Fahad Ehsan, M., Naeem Ashiq, M., Ijaz, S., Najam-ul-Haq, M., Hamid, S., Bahnemann, D.W., 2019. Synthesis, characterization and photocatalytic activity of $LaNdZr_2O_7$ supported SnSe nanocomposites for the degradation of Foron blue dye. Appl. Surf. Sci. 463, 1019–1027.

Taneja, P., Sharma, S., Umar, A., Mehta, S.K., Ibhadon, A.O., Kansal, S.K., 2018. Visible-light driven photocatalytic degradation of brilliant green dye based on cobalt tungstate ($CoWO_4$) nanoparticles. Mater. Chem. Phys. 211, 335–342.

Saha, M., Ghosh, S., De, S.K., 2020. Nanoscale Kirkendall Effect Driven Au Decorated CdS/CdO Colloidal Nanocomposites for Efficient Hydrogen Evolution, Photocatalytic Dye Degradation and Cr (VI) Reduction. Catal. Today. 340, 253–267.

Mechouche, M.S., Merouane, F., Messaad, C.E.H., Golzadeh, N., Vasseghian, Y., Berkani, M., 2021. Biosynthesis, characterization, and evaluation of antibacterial and photocatalytic methylene blue dye degradation activities of silver nanoparticles from Streptomyces tuirus strain. Environ. Res. 112360.

Almehizia, A.A., Al-Omar, M.A., Naglah, A.M., Bhat, M.A., Al-Shakliah, N.S., 2021. Facile synthesis and characterization of ZnO nanoparticles for studying their biological activities and photocatalytic degradation properties toward methylene blue dye. Alexandria Eng. J. https://doi.org/10.1016/j.aej.2021.06.102.

Stanley, R., Jebasingh, J.A., Stanley, P.K., Ponmani, P., Shekinah, M. E., Vasanthi, J., (2021). Excellent Photocatalytic degradation of Methylene Blue, Rhodamine B and Methyl Orange dyes by Ag-ZnO nanocomposite under natural sunlight irradiation. Optik (Stuttg) 231.

Chakraborty, U., Bhanjana, G., Kannu, N., Kaur, R., Sharma, G., Kaur, A., Kaushik, G.R.C., 2021. Microwave-assisted assembly of $Ag_2O$-ZnO composite nanocones for electrochemical detection of 4-Nitrophenol and assessment of their photocatalytic activity towards degradation of 4-Nitrophenol and Methylene blue dye. J. Hazard. Mater. 416, 125771.

Kim, J., Lee, J., Liu, C., Pandey, S., Woo Joo, S., Son, N., Kang, M., 2021. Achieving a long-term stability by self-redox property between Fe and Mn ions in the iron-manganese spinel structured electrode in oxygen evolution reaction. Appl. Surf. Sci. 546, 149124.

Arshad, R., Barani, M., Rahdar, A., Sargazi, S., Cucchiarini, M., Pandey, S., Kang, M., 2021. Multi-functionalized nanomaterials and nanoparticles for diagnosis and treatment of retinoblastoma. Biosensors 11, 1–19.

Sabir, F., Zeeshan, M., Laraib, U., Barani, M., Rahdar, A., Cucchiarini, M., Pandey, S., 2021. Dna based and stimuli-responsive smart nanocarrier for diagnosis and treatment of cancer. Appl. Challenges.

Sargazi, S., Hajinezhad, M.R., Barani, M., Rahdar, A., Shahraki, S., Karimi, P., Cucchiarini, M., Khatami, M., Pandey, S., 2021. Synthesis, characterization, toxicity and morphology assessments of newly prepared microemulsion systems for delivery of valproic acid. J. Mol. Liq. 338, 116625.

Hegazey, R.M., Abdelrahman, E.A., Kotp, Y.H., Hameed, A.M., Subaihi, A., 2019. Facile fabrication of hematite nanoparticles from Egyptian insecticide cans for efficient photocatalytic degradation of rhodamine B dye. J. Mater. Res. Technol. 9, 1652–1661.

Alharbi, A., Abdelrahman, E.A., 2020. Efficient photocatalytic degradation of malachite green dye using facilely synthesized hematite nanoparticles from Egyptian insecticide cans, Spectrochim. Acta Part A Mol. Biomol. Spectrosc. 226, 117612.

Abdelrahman, E.A., Hegazey, R.M., Kotp, Y.H., Alharbi, A., 2019. Facile synthesis of Fe2O3 nanoparticles from Egyptian insecticide cans for efficient photocatalytic degradation of methylene blue and crystal violet dyes. Spectrochim. Acta - Part A Mol. Biomol. Spectrosc. 222, 117195.

M.C. Jayaprakash, M. Chaitra, P. Rai, D. Venkat Reddy, Removal of Methylene Blue from Aqueous Solution: An Approach of Environmental Friendly Activated Carbon, Springer International Publishing, 2021. Doi:10.1007/978-3-030-51354-2_16.

Pu, A., Deng, J., Hao, Y., Sun, X., Zhong, J., 2014. Thickness effect of hematite nanostructures prepared by hydrothermal method for solar water splitting. Appl. Surf. Sci. 320, 213–217.

Yang, H.M., Ma, S.Y., Yang, G.J., Jin, W.X., Wang, T.T., Jiang, X. H., Li, W.Q., 2016. High sensitive and low concentration detection of methanol by a gas sensor based on one-step synthesis α-$Fe_2O_3$ hollow spheres. Mater. Lett. 169, 73–76.

Lassoued, A., Lassoued, M.S., Dkhil, B., Ammar, S., Gadri, A., 2018. Synthesis, photoluminescence and Magnetic properties of iron oxide (α-$Fe_2O_3$) nanoparticles through precipitation or hydrothermal methods. Phys. E Low-Dimensional Syst. Nanostruct. 101, 212–219.

Liang, H., Liu, K., Ni, Y., 2017. Synthesis of mesoporous α-$Fe_2O_3$ using cellulose nanocrystals as template and its use for the removal of phosphate from wastewater. J. Taiwan Inst. Chem. Eng. 71, 474–479.

Davar, F., Hadadzadeh, H., Alaedini, T.S., 2016. Single-phase hematite nanoparticles: Non-alkoxide sol–gel based preparation, modification and characterization. Ceram. Int. 42, 19336–19342.

Supattarasakda, K., Petcharoen, K., Permpool, T., Sirivat, A., Lerdwijitjarud, W., 2013. Control of hematite nanoparticle size and shape by the chemical precipitation method. Powder Technol. 249, 353–359.

Yang, T., Wang, D., Zhai, C., Luo, Y., Zhang, M., 2018. Ultrafast response and recovery of single crystalline α-$Fe_2O_3$ nanorhombohedrons for trimethylamine sensing applications. Mater. Lett. 210, 1–3.

Wang, J., Houwman, E., Salm, C., Nguyen, M., Vergeer, K., Schmitz, J., 2017. Process induced poling and plasma induced damage of thin film PZT. Microelectron. Eng. 177, 13–18.

De Faria, D.L.A., Venâncio Silva, S., De Oliveira, M.T., 1997. Raman microspectroscopy of some iron oxides and oxyhydroxides. J. Raman Spectrosc. 28, 873–878.

Fei, X., Shao, Z., Chen, X., 2013. Hematite nanostructures synthesized by a silk fibroin-assisted hydrothermal method. J. Mater. Chem. B. 1, 213–220.

Su, X., Yu, C., Qiang, C., 2011. Synthesis of α-$Fe_2O_3$ nanobelts and nanoflakes by thermal oxidation and study to their magnetic properties. Appl. Surf. Sci. 257, 9014–9018.

Xu, Y.Y., Zhao, D., Zhang, X.J., Jin, W.T., Kashkarov, P., Zhang, H., 2009. Synthesis and characterization of single-crystalline α-$Fe_2O_3$ nanoleaves. Phys. E Low-Dimensional Syst. Nanostruct. 41, 806–811.

Dong, B., Yu, X., Dong, Z., Yang, X., Wu, Y., 2017. Facile synthesis of ZnO nanoparticles for the photocatalytic degradation of methylene blue. J. Sol-Gel Sci. Technol. 82, 167–176.

Al-Wasidi, A.S., AlZahrani, I.I.S., Thawibaraka, H.I., Naglah, A.M., AlReshaidan, S., Youssef, H.M., 2021. Facile Hydrothermal Synthesis of Copper Chromite Nanoparticles for Efficient Photocatalytic Degradation of Acid Orange 7 Dye. J. Inorg. Organomet. Polym. Mater. https://doi.org/10.1007/s10904-021-02113-y.

Kotp, Y.H., 2021. High-flux TFN nanofiltration membranes incorporated with Camphor-$Al_2O_3$ nanoparticles for brackish water desalination. Chemosphere 265, 128999.

Kotp, Y.H., 2019. Removal of organic pollutants using polysulfone ultrafiltration membrane containing polystyrene silicomolybdate nanoparticles: Case study: Borg El Arab area. J. Water Process Eng. 30, 100553.

El-Aassar, A.H.M., Abo Elfadl, M.M.S., Ali, M.E.A., Kotp, Y.H., Shawky, H.A., 2017. Effect of manufacture conditions on reverse osmosis desalination performance of polyamide thin film composite membrane and their spiral wound element. Desalin. Water Treat. 69, 65–71.

Shawky, H.A., Yaseen, R., Kotp, Y.H., Eissa, D., 2020. Biosynthesis of silver nanoparticles and its effect on TFC RO membrane for groundwater desalination. Desalin. Water Treat. 193, 34–47.